Silicon (2019) 11:2505–2515
https://doi.org/10.1007/s12633-019-00137-1

ORIGINAL PAPER

# Study of Structural, Electronic and Vibrational Properties of Porous Silicon with Different Porosity

H. Lachenani[1,2] · A. Larabi[2] · N. Gabouze[2]

Received: 10 October 2018 / Accepted: 13 March 2019 / Published online: 21 March 2019


**Abstract**
In this work, density functional theory (DFT) was utilized to study the influence of the porosity on the structural, electronic and vibrational properties of porous silicon (PS). It is based on the potential plane wave (PP-PW) method within generalized gradient approximation (GGA). Supercell model was used to simulate nanopores structures. The results obtained from the formation energy calculation exhibited that the most stable structure corresponds to the highest porosity (40.62%). Moreover, a direct band gap is calculated for all porosities and enlargement of energy gap with porosity was observed. The obtained IR spectra calculation show a resemblance between 15.62 and 40.62% porosities and 3.12 and 28.12% porosities. In order to confirm the theoretical results, we prepared porous silicon specimens by electrochemical etching of (001) p-type silicon wafer (1–10 Ohm cm resistivity). In addition, the IR spectra of PS layers were measured and compared against the calculated spectra. IR absorbance spectrum obtained for a porosity of 40.62% shows great agreement with the experimental one and confirms that the surface is hydrogenated.

**Keywords** Porous silicon · IRFT · Ab-initio · Hydrogen passivation

## 1 Introduction

During the last decades, the interest in the development of porous silicon films has stimulated many researchers to work on electrical, optical and various properties of this material. It is well established that porous silicon (PS) is a promising material for several applications in significant and varied fields (photoluminescence (PL), electroluminescence (EL), gas and (bio) sensing, depollution, etc.). Since its discovery by Turner [1], porous silicon realized by the anodic etching of crystalline silicon in hydrofluoric acid has been extensively investigated. Anodic oxidation of silicon is connected with the consumption of holes at the surface. Indeed, the electrochemical dissolution of porous silicon in hydrofluoric acid solutions leads to the hydrogen-terminated surface (Si-$H_x$ x = 1, 2, 3). In addition, using the electrochemical etching of silicon, the porosity of silicon can be varied from less 1% to as high as 97% [2]. It is a critical parameter for applications such as drug delivery [3], sensing [4], photoluminescence [5], etc. It also has a dramatic effect on mechanical properties such as strength and hardness [6, 7], thermal and optical properties such as conductivity [8] and refractive index [9], respectively. Since the discovery of visible photoluminescence (PL) at room temperature from porous silicon (PS) by Canham in 1990 [5], about several thousand papers were published in the field. This high activity has also gained interest for the electrochemical study of the interface of silicon-fluoride medium [10, 11]. Slimani et al have experimentally studied the macropore creation in p-type silicon in a HF solution and the transition between macropore formation and electropolishing. [12]. In addition, to represent the anodic dissolution of p-type Si in HF/ electrolyte within

✉ A. Larabi
amina.larabi8@gmail.com

[1] Laboratoire de Physique des Techniques Expérimentales et ses Applications de Médéa LPTEAM, Département Science de la Matière, Faculté des Sciences, Université de Médéa, Médéa, Algeria

[2] Centre de Recherche en Technologie des Semi-conducteurs pour l'Energétique (CRTSE), 02 Bd, Frantz Fanon, B.P, 140 Alger, Algeria

the first plateau of the electropolishing zone a mathematical model has been developed by Cheggou et al. [13]. Moreover, using a modified diffusion limited aggregation model, Matthai et al. have simulated the porous silicon structure obtained by anodic etching [14]. However, there have been few theoretical works devoted to understand the effect of the hydrogen-terminated surface (Si-H) on structural, electronic, vibrational and optical properties. The simulation of a porous material presenting different structures is not clearly described, and constitutes a very difficult but interesting challenge. Really, from a theoretical perspective, modeling of microscopic porous structures is a challenging charge [15].

Two options can be used: semi-empirical method, like empirical pseudopotentials and tight-binding (TB) which are founded on atomic orbitals, and ab-initio methods, through DFT with GW correction or quantum Monte Carlo calculations [15]. The former presents the advantage to be easy and able to resolve the complex porous structures and it is suitable for the study of hydrogen passivation of silicon. Instead, the ab-initio calculations, which are more accurate, treat only simple porous structures.

In this work, structural, electronic and vibrational properties investigations of PS were performed using ab-initio pseudo potential plane wave (PP-PW) method founded on DFT described by the generalized gradient approximation (GGA) included in the CASTEP program (Cambridge Serial Total Energy Package) [16, 17]. Furthermore, the computation of IR absorption spectra needs the calculation of atomic vibrational modes, which was performed by the DFPT. The IR spectra of hydrogenated PS layers were measured and compared with the calculated spectra.

## 2 Computational Details

Supercell model was used to simulate nanopores in porous silicon structure [18, 19] by taking out columns of atoms in the [0 0 1] direction on c-Si crystal. We begin from a supercell of 32 atoms formed by connecting four cubic cells, each with eight Si-atoms and lattice constant a = 5.43 Å. The lattice constants of the supercell (2x2x1) are of A = B = 2a and C = a.

To obtain different porosities P (ratio between the number of removed atoms to their total in the supercell), number of 1, 5, 9, 13 and 15 central Si atoms were removed from the supercell, which produced a porosity of 3.12, 15.62, 28.12, 40.62 and 46.87% successively as illustrated in Fig. 1. These chosen porosities ensure the same square shape of the pore along z-axis and the same space group $P\overline{4}$ 2 m (N°.111) for different tetragonal structures studied. H atoms were used to passivate all surfaces dangling bonds in silicon pores [20]. Ab-initio pseudo potential plane wave (PP-PW) method founded on DFT (implemented in the CASTEP software) was employed to accomplish structural and electronic properties of PS.

The exchange correlation effect was processed using the generalized gradient approximation developed by Perdew-Burke-Ernzerhof (GGA-PBE) function. The pseudopotential of Vanderbilt-type ultra-soft was utilised to compute the potential seen by the valence electrons. Valence electronic wave functions were expanded in a plane-wave basis set truncated at a maximum plane-wave energy of $E_{cut\text{-}off}$ = 900 eV. Brillouin zone integrals were converged with 1x1x3 Monkhorst-Pack k-point mesh [21], which was sufficient to ensure energy convergence for (2x2x1) supercell. All structures were optimized to their basal state by modifying the atomic coordinates and the supercell shape through the Broyden– Fletcher–Goldfarb–Shanno BFGS algorithm [22, 23]. The convergence tolerance was fixed to $10^{-7}$ eV/atom for energy, 0.002 eV/Å for maximum force, 0.02 Gp for maximum stress, and $10^{-5}$ Å for maximum displacement.

The vibrational modes and the IR absorption spectra were calculated using DFPT and norm-conserving pseudopotentials with the same convergence criteria [24].

## 3 Experimental Procedure

In order to confirm the ab-initio results, nanoporous silicon specimens were processed. Porous silicon (PS) was achieved by electrochemical etching of (001) p-type silicon wafer (1–10 Ohm cm resistivity). The pro The Ohmic contact on the back side of the Si anode has been achieved by rubbing GaIn eutectic. Anodization of p-type substrates was performed under galvanostatic conditions in a simple O-ring cell in the dark, with a Pt wire as counter electrode and saturated calomel electrode as reference (SCE) using a Biologic VMP3 potentiostat/galvanostat as described elsewhere (Fig. 2**)** [25]**.** The etching solution was prepared by adding 30 vol.% of ethanol to 70 vol.% of HF aqueous solution (49 wt.%). The wafer was etched at a current density of 10 mA/cm$^2$ and etching time of 5mn to obtain a porosity of approximately 40% [26, 27]. The IR spectra of the prepared samples were measured by a thermo Nicolet Nexus FTIR Spectrometer. All FT-IR spectra were registered in absorbance mode in the IR region 400–4000 cm$^{-1}$ at 4 cm$^{-1}$ resolution.

## 4 Results and Discussion

### 4.1 Structural Properties

The step of geometry optimization of all studied structures conducts to the optimized structural parameters mainly, the

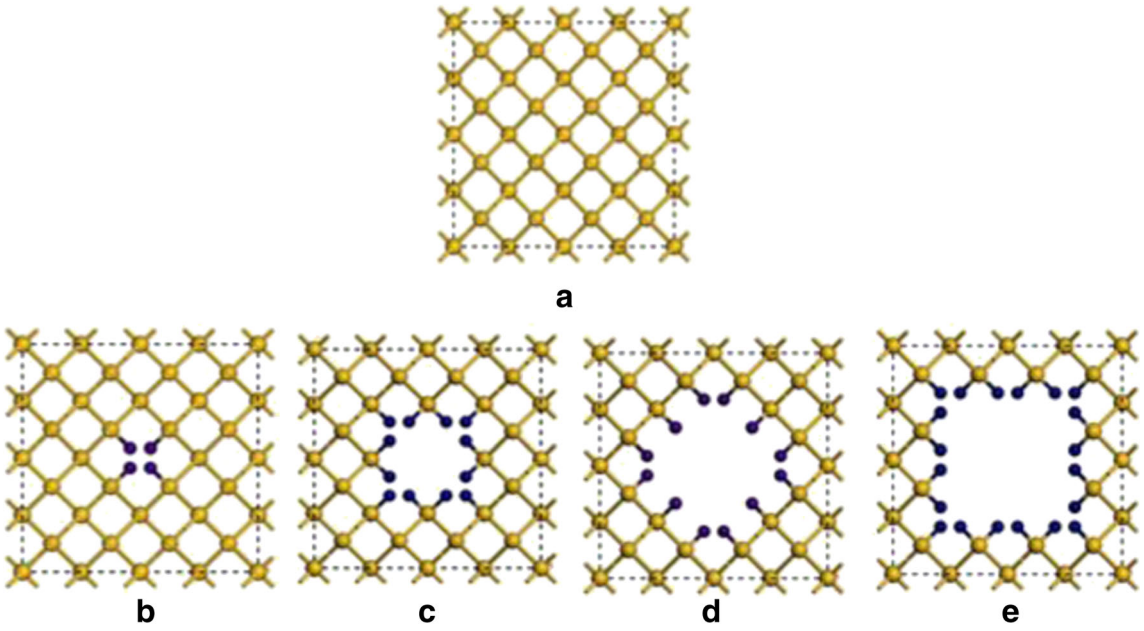


**Fig. 1** Porous silicon model where yellow and blue spheres represent Si and H atoms, respectively. A represents 32 atoms supercell of c-Si, and B, C, D and E are full H passivated porous silicon with 3.125%, 15.625%, 28.125%, and 40.625% of porosity, respectively

lattice constant (A, B, C), the angle (α, β, γ), and the unit-cell volume V for tetragonal structures. For each porosity, at zero pressure, the precedent parameters are reported in Table 1.

For the porosity of 46.87%, we observe a distortion and phase transition in this structure. This constitutes the limit of the porosity that can be created in the chosen supercell. In fact, the selected size of the supercell model imposes a limit to the number of removed Si atoms.

A good accord was observed between theoretical and experimental lattice constants of the c-Si [28]. A very small

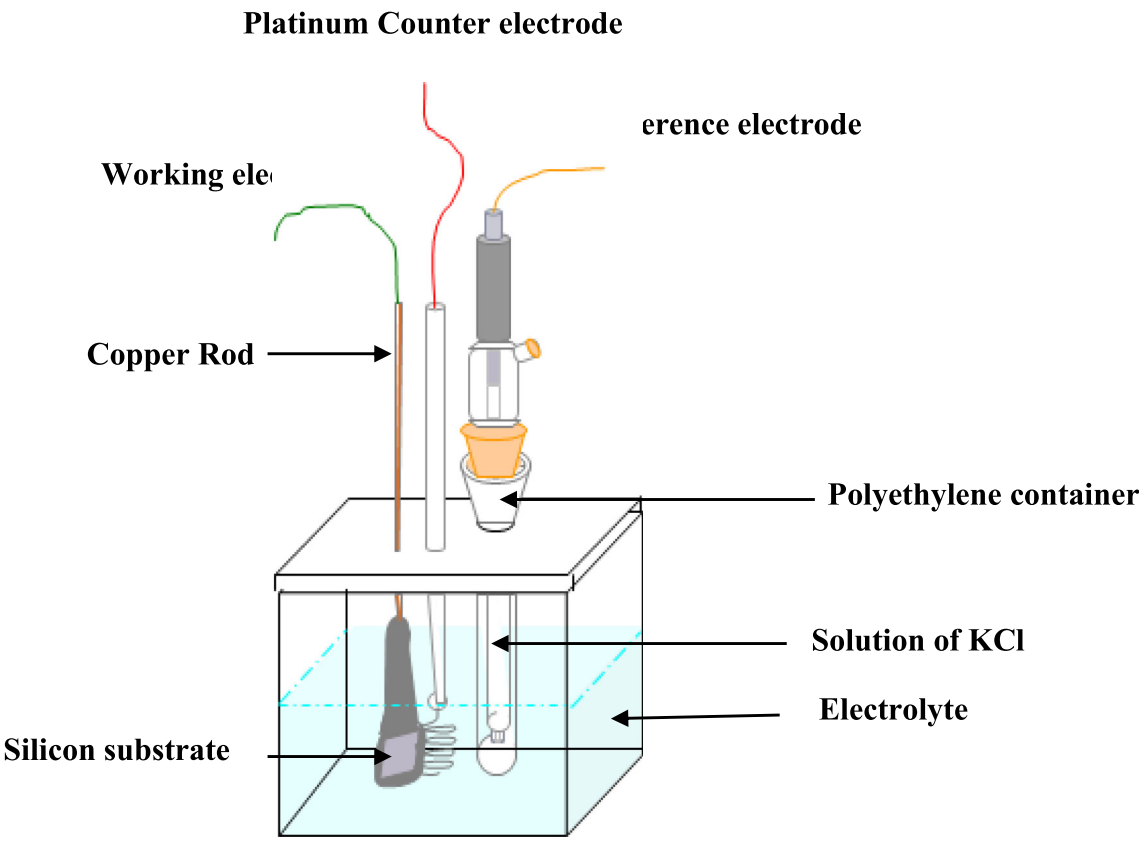


**Fig. 2** Anodization cell used for porous silicon elaboration [25]

**Table 1** The variation of the lattice parameters (A, B, C), the angles (α, β, γ) and the unit-cell volume *V* for each porosity

| | | Lattice parameters (Å). | | Volume V (Å$^3$). | Angle(α,β,γ) (deg) |
|---|---|---|---|---|---|
| | | A = B | C | | |
| Bulk Si (cSi) | | 10.880 | 5.440 | 644.030 | 90 |
| Porosity (P) % | 3.12% | 11.023 | 5.453 | 662.667 | 90 |
| | 15.62% | 11.205 | 5.487 | 688.933 | 90 |
| | 28.12% | 11.014 | 5.526 | 670.293 | 90 |
| | 40.62% | 12.012 | 5.174 | 746.459 | 90 |
| | 46.87% | A = 9.6796<br>B = 4.966 | 12.360 | 590.680 | α = γ = 90 deg.<br>β =83.85 deg |

relative difference (0.16%) was observed between the calculated value (5.44 Å) and measured value (5.43 Å). For all porosities, the PS structures expand when compared to that of c-Si due to the hydrogen-hydrogen interaction as notified by Cisneros et al. [29].

The obtained supercell volume from GGA for all porosities **rises** with the increase of porosity when the form and orientation of the pore are similar. Actually, there are two different orientations of our chosen pore shape. The first one for 3.12 and 28.12% structures (orientation 45 deg.) and the second one for 15.62 and 40.62% structures (orientation 0 deg.).

To illustrate the effect of the porosity on the stability of the PS structure; we have calculated the formation energies $E_f$ by the expression [18]:

$$E_f = E_{PS} - \sum_{i=Si,H} n_i u_i \quad (1)$$

Where $E_{PS}$ is the ground-state energy (total energy) of the passivated PS, $n_i$ indicates the number of the atomic species per supercell, and $\mu_i$ is the chemical potential of the atomic species. The chemical atomic potential, which is negative for a stable compound is obtained in the ground-state bulk phase of Si. The chemical potential of hydrogen $\mu_H$ is determined from half of $H_2$ molecule energy.

After the step of geometry optimization of all studied structures, the values of calculated formation energy for all porosity used are shown in Fig. 3. It shows that all formation energies are negative, indicating favourable structures. The lowest energy value corresponds to the structure having the porosity of 40.62%, which is the most stable.

Unfortunately, attempts to increase porosity over this value were failed due to the reduced atoms number in the 32 atoms supercell.

## 4.2 Electronic Properties

Figure 6 shows the band structures in the Brillouin zone (BZ) for high-symmetry points of Si crystal and PS with different porosity. The corresponding points of high symmetry, *k*-point paths, in BZ (Fig. 4) are: Z(0, 0, 0.5) →

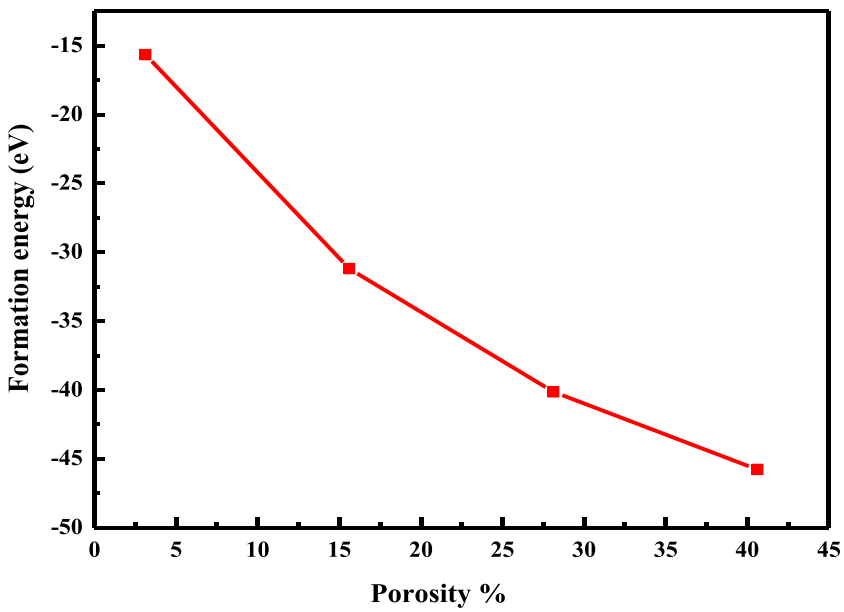


**Fig. 3** Formation energy trends vs porosity for full H passivation

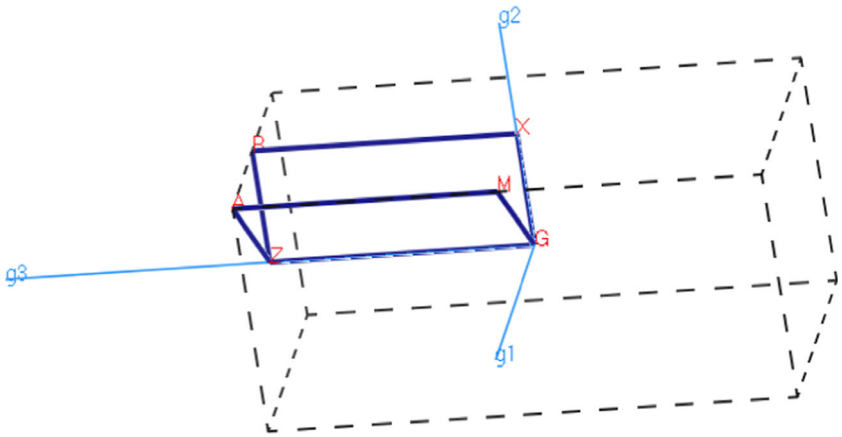


**Fig. 4** Brillouin zone of the porous silicon. The high symmetry line of the band structure is represented by the blue line

A(0.5, 0.5, 0.5) → M(0.5, 0.5, 0) → G(Γ)(0, 0, 0) → Z(0, 0, 0.5) → R(0, 0.5, 0) → X(0, 0.5, 0) → G(0, 0, 0).

The band gap energy $E_g$ was determined as the difference between the highest point level and the lowest point of valence band (HVB) and conduction band (LCB), respectively. The calculated $E_g$ value is 0.575 eV for bulk Si indicating an indirect band gap because both HVB and LCB were located on different symmetry points in the Brillouin zone.

Comparison between the experimental band gap for bulk Si, 1.12 eV [27] and calculated value, 0.575 eV shows an underestimation. This is well known and obtained systemically in GGA. Nevertheless, this result has no impact on the energy band and electronic structure analyses.

To examine how the band gap of PS changes with the porosity, we plotted in Fig. 5 the total and projected density of states (TDOS and PDOS) calculated for c-Si and PS. In this figure, the vertical dashed line illustrates the Fermi energy level. We can observe from Fig. 4a, b, that the calculated PDOS in the valence band is separated into two zones; the first zone from −12.5 to −5 eV displays a strong influence coming from states of Si (s-Si), with a minor influence of p states (p-Si). The second part from −5 to 0 eV results from p-Si states with a little role of s-Si states. The conduction band results from p-Si states and a minor part of contribution depends from s-Si. Compared to pure Si (Fig. 5a), for the different porosity (Fig.5c, d, e, f) we note an increase of band gap widths.

The electron band structures (Figs. 6c-f) show, for the different porosity, the feature of direct band gap in contrary to the c-Si (Figs. 6a), which possesses an indirect band gap. This was caused by the supercell model when a big unit cell conducts to folding of the Brillouin zone where its size is reduced (Figs. 6b). This causes the lowest point of the c-Si conduction band to move towards the centre of the Brillouin zone, which makes the band gap turns into direct [30]. This feature was also found by Cisneros et al. [28]. Moreover, Trejo et al. [20] mentioned this observation and reported that this direct band gap was not only observed in supercell model but occurs in real porous semiconductors too. They suggested that, particularly in PS with high porosity, the existence of interconnection column skeleton producing alternative connections, which induces carriers and could find paths from one nanopore to others.

Otherwise, as shown in Fig. 6, an increase in porosity leads to the increase in the band gap energy values. It is noticeable that higher porosity needs higher formation energy to be created with greater quantum confinement in the resulting structure.

To define the relationship between enlargement of the band gap Eg, the width of the pore (d) and the confinement distance between pore boundaries (L), we have chosen porosities leading to the same square shape and symmetry as mentioned in Figs. 7 and 8.

A linear trend between energy band gap and the width of pores is observed (Fig. 9). The positive slope confirms that the band gap increases with porosity and pore width. The broadening of porous silicon band gap with the porosity is attributed to the effect of the pore surfaces on electron wave functions which cause a sort of quantum confinement and consequently a band-gap broadening [31]. Finally, wave functions with wavelengths wider than the distance between nodes will not be reachable for the system [32]. In addition, Zhe Chuan Feng and Raphael Tsu [33], attributed the broadening observed at lower porosities to the reduction in effective crystallite size and it may also be due to loss of long-range order due to misorientation and microscopic stress. Moreover, the enlargement of the band gap was shown when the confinement distance between pore boundary decreases as reported in Fig. 9. This is in agreement with other cases of Si porous structures [20] where for high porosity, when pores touch each other (L become small), the quantum confinement becomes complete [34].

After the geometrical optimization, calculation of the vibrational modes and the IR absorption spectra were performed by DFPT [24]. IR spectra for different porosity with full H passivation are shown in Fig. 10. It can be divided in three ranges (Table 2). In the wavenumber range of 2000–2300 $cm^{-1}$, for all porosities the calculated IR indicates the

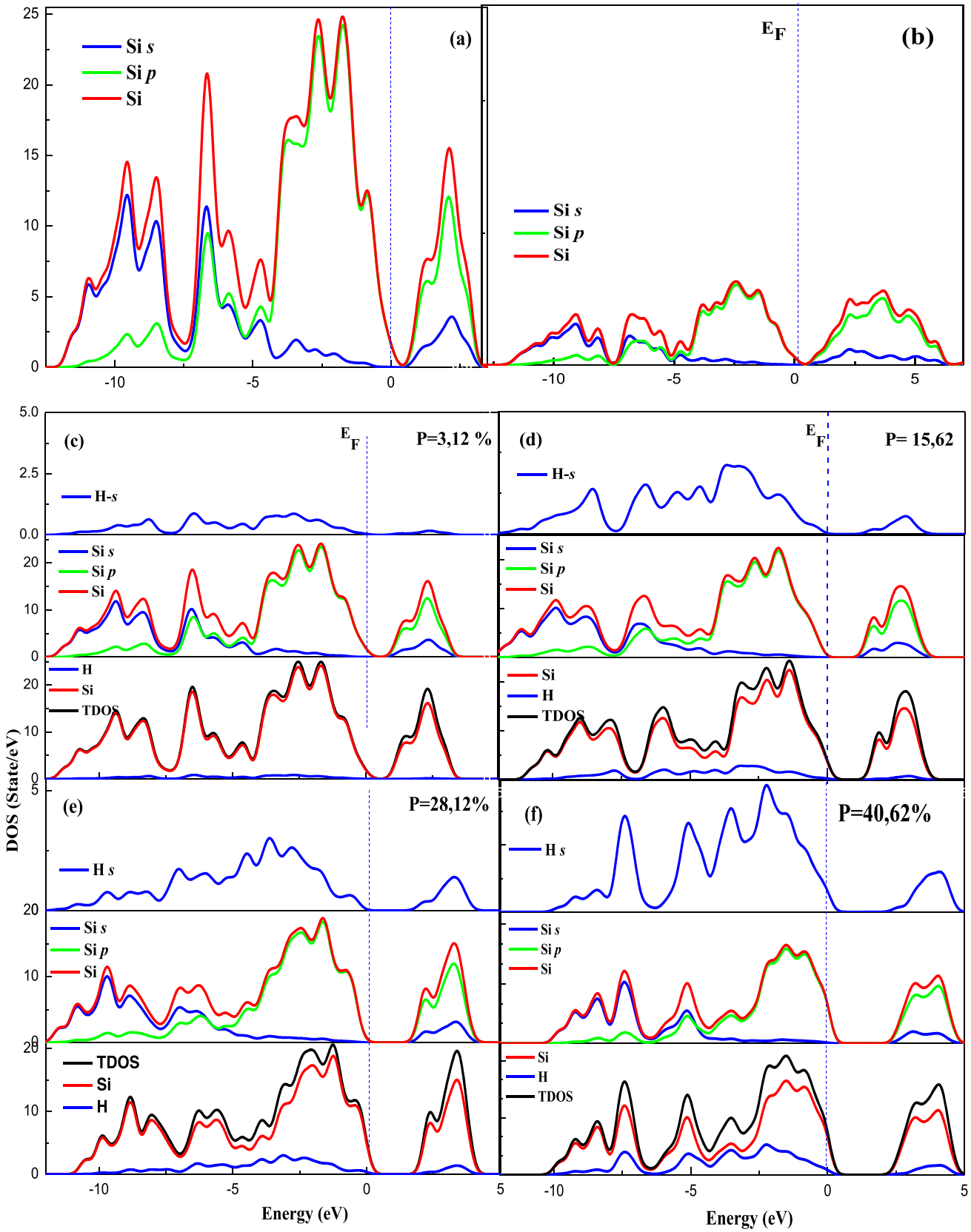


**Fig. 5** Total density of state (TDOS) and partial density of state (PDOS) projected onto s and p orbitals for Si and H atoms for a) bulk Si, b) Si supercell (2*2*1), c, d, e and f) porous silicon with 3.125, 15.625, 28.125, 40.625% porosity, respectively. The vertical dashed line corresponds to the Fermi level

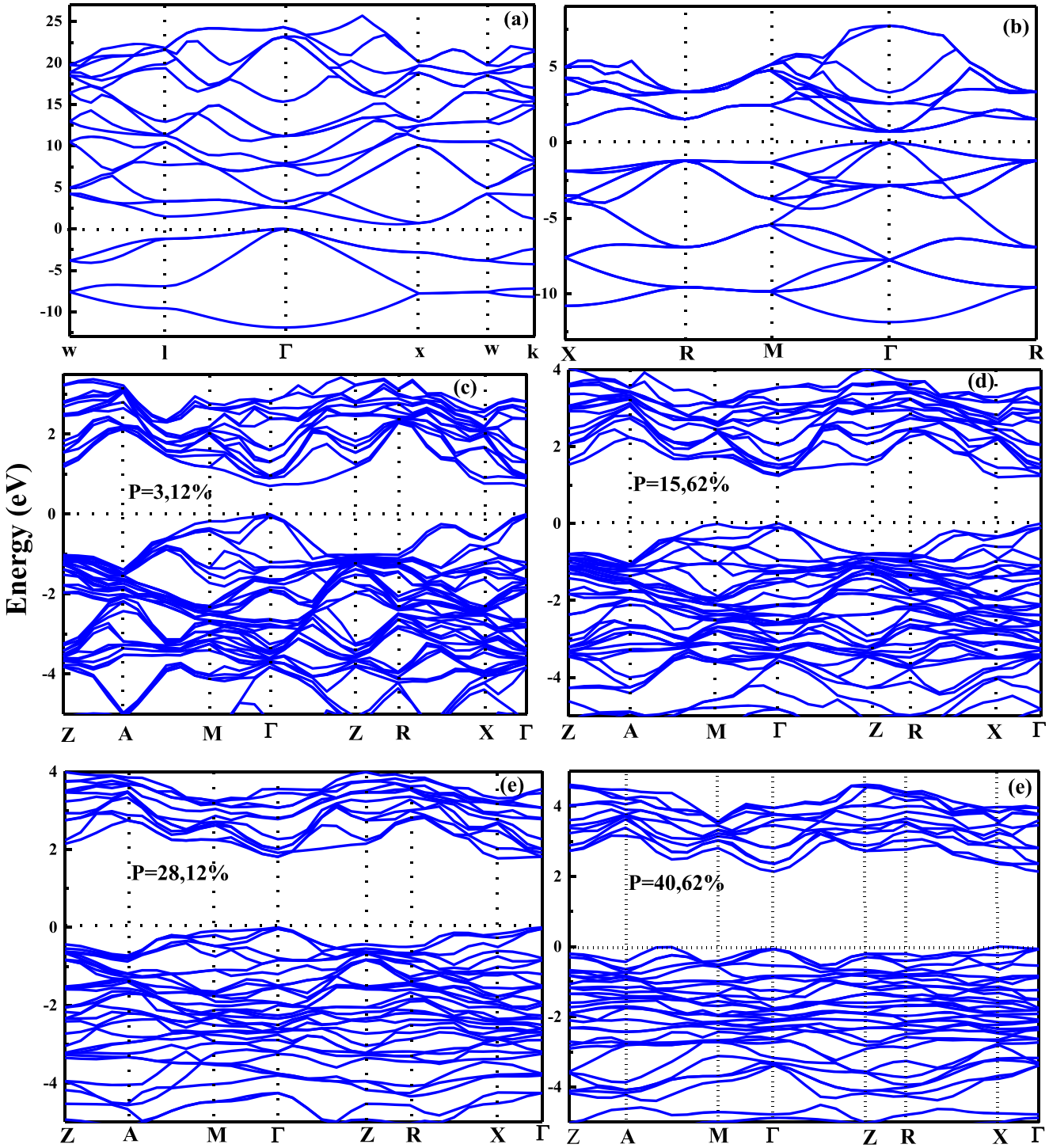


**Fig. 6** Electronic band structure for a) bulk Si, b) bulk Si with supercell model (2*2*1), c, d, e and f porous silicon with 3.12, 15.62, 28.12, 40.62% porosity, respectively

presence of relatively high intense peaks, with some shifting corresponding to Si-H stretching band. For the two porosities of 40.62 and 15.62%, we observe other peaks, which can be attributed to $SiH_2$ bonding.

The second narrow range comprised between 840 $cm^{-1}$ and 900 $cm^{-1}$, observed only for the two porosities of 15.62 and 40.62%, shows single peak with slight shifting, assigned to the presence of $SiH_2$ bonding. The third wavenumber range comprised between 590 and 680 $cm^{-1}$ is present for all porosity. The principal peak showing a high intensity is assigned to Si-Si vibration. We note that other weak peaks, which can be attributed to $SiH_x$ bonding, are also present in this range. In this zone, we also observe a shift in the absorbance peak to higher wavenumbers when the porosity increases. This is

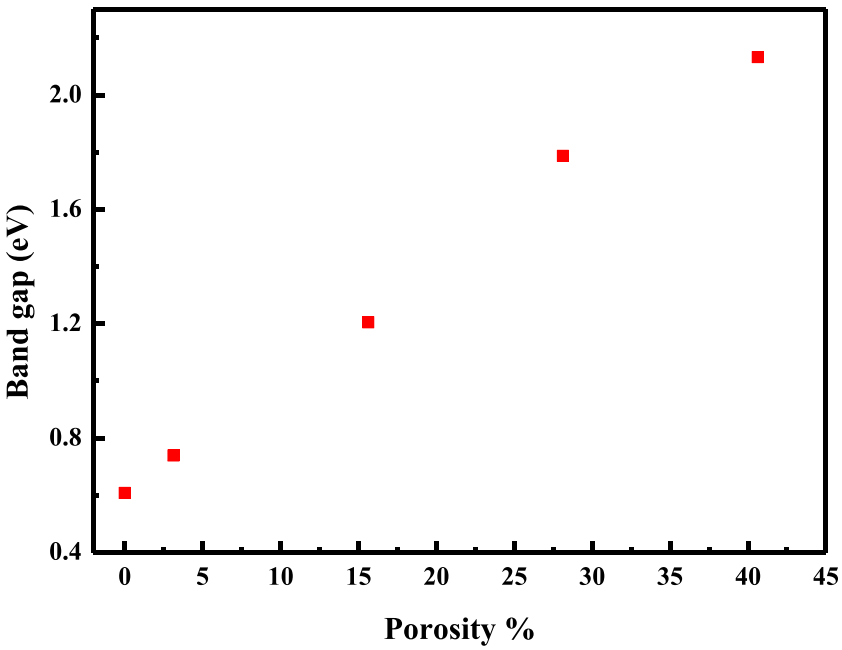


**Fig. 7** Evolution of band gap energy with porosity

probably due to the different orientation of the pore shape created in the chosen studied supercell.

Figure 11 shows, the FTIR spectrum measured from Si sample anodized at current density of 20 mA/cm$^2$ and etching time 20 min. The FTIR absorption spectrum in the range 580–640 cm$^{-1}$ of a PS layer depicts intense peaks at 607 and 617 cm$^{-1}$, which are assigned to Si–C and Si–Si stretching modes, respectively [35] and a peak at 628 cm$^{-1}$ attributed to bond-bending mode of Si-H [36] which is close to Si-Si vibration. The peak at

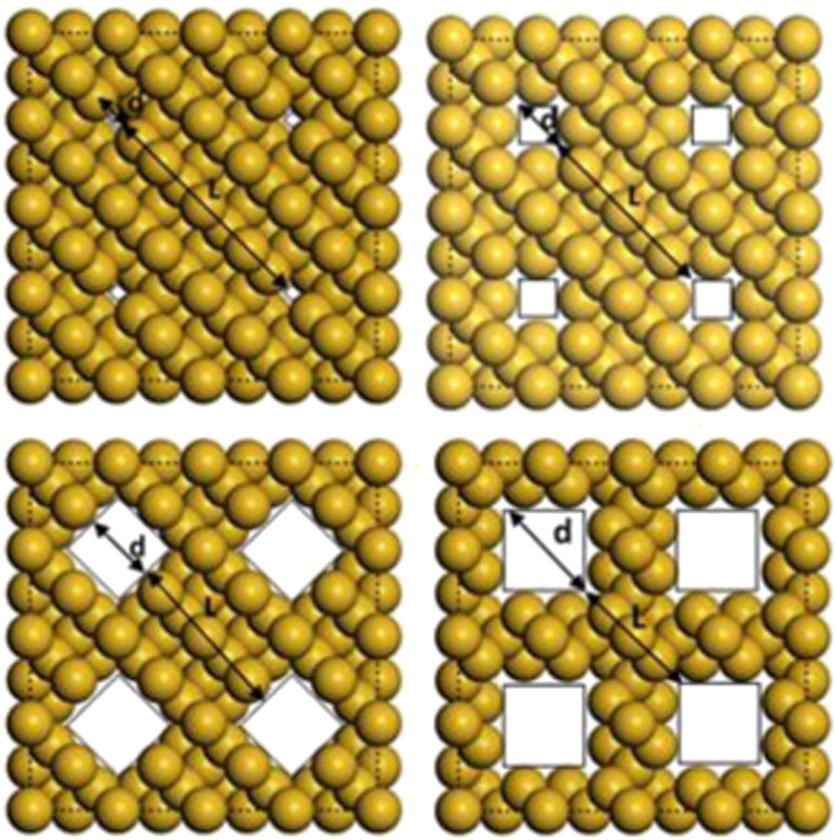


**Fig. 8** Pores width (d) and confinement distance (L) between pore boundaries for different porosities for a) $P = 3.25\%$; b) $P = 15.62\%$; c) $P = 28.12\%$; d) P = 40.62%

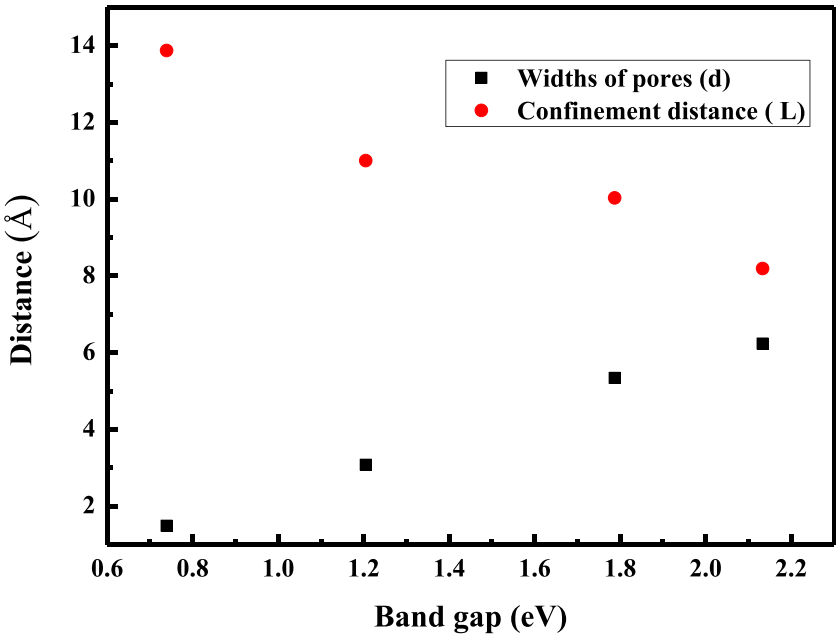


**Fig. 9** Variation of energy band gap of PS as a function of pore widths and confinement distance between pore boundaries

675 $cm^{-1}$ is assigned to stretching mode of Si-$H_2$. In addition, the spectrum displays characteristic peaks of the Si-H stretching modes, namely, the bands at 2085 $cm^{-1}$, 2115 $cm^{-1}$and 2140 $cm^{-1}$ ascribed to monohydride, dihydride and trihydride contributions, respectively. The corresponding bending modes of Si-$H_2$ bond is observed at 908 $cm^{-1}$ (scissor mode) [35, 37, 38]. The presence of $SiH_x$ bands in the IR spectrum are characteristics of porous silicon. We notice that the PS surface is oxide free due to the absence of any significant contribution in the 1000–1200 $cm^{-1}$ range [33, 34]. In addition, the spectrum reveals also the absence of a broad OH stretching vibration band ν(OH) in the 300–3600 $cm^{-1}$ indicating no traces of water into the pore. One can note that all the attributed IR bands and peaks are in good agreement with those obtained in the literature (reported in Table 3).

Moreover, the comparison of the calculated vibrational properties of porous silicon with a porosity $P = 40.62\%$ with experimental IR bands acquired from porous silicon with a porosity of about 40% were found in good agreement as shown in Table 3.

In comparison with experimental FTIR data, the vibrational band of $SiH_3$ does not appear in this

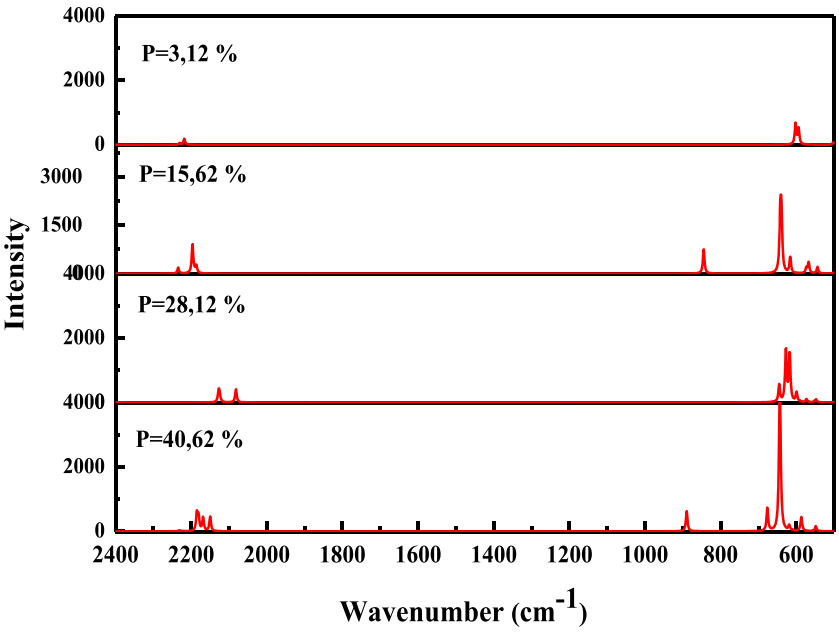


**Fig. 10** IR vibrational spectra for porous silicon with different porosities

**Table 2** Main IR vibrational frequencies of PS

| Bonds | Frequency ($cm^{-1}$) | | | |
|---|---|---|---|---|
| | Porosity (This calculation) | | | |
| | 3.125% | 15.625% | 28.125% | 40.625% |
| Si-Si | 594.13 | 639.64 | 627.75 | 642.32 |
| SiH | 602.23 | 616.29 | 617.84 | 644.20 |
| $SiH_2$ | | 642.55 | | 676.73 |
| $SiH_2$ | / | 845.01 | / | 889.92 |
| SiH | 2218.24 | 2196.41 | 2127.75 | 2149.89 |
| $SiH_2$ | / | 2185.97 | / | 2184.83 |

**Table 3** Main IR vibrational frequencies of PS with $p = 40.625\%$

| Bonds | Frequency ($cm^{-1}$) | | |
|---|---|---|---|
| | Porous silicon with p = 40.625% (This calculation) | Experimental (This work) | Ref |
| Si-Si | 642.32 | 617 | 620 [34] |
| SiH | 644.20 | 628 | 626 [35] |
| $SiH_2$ | 676.73 | 666–675 | 662 [35] |
| $SiH_2$ | 889.92 | 908 | 880–910 [35–37] |
| SiH | 2149.89 | 2085 | 2084–2112 [33, 34, 37] |
| $SiH_2$ | 2184.83 | 2115 | 2082–2121 [34, 35, 37, 38] |
| $SiH_3$ | / | 2140 | 2130–2140 [35, 36] |

calculation. In fact, the process of creating pores in the chosen supercell model while respecting the symmetry does not allow the formation of $SiH_3$.

## 5 Conclusion

In this paper, we have performed an ab initio quantum mechanical study of the hydrogen effects and porosity variation on the PS structure and its electronic and vibrational properties. Structural, vibrational and electronic properties study of PS were performed using pseudo potential plane wave (PP-PW) method founded on the DFT with the GGA-PBE approach.

The formation energies obtained from DFT calculation confirm that the stability of PS structure is related to its porosity and high porosities have the lowest energy formation values. In addition, the electronic band structure of all PS structure shows direct band gap semiconductors for all studied porosities.

The calculated IR in the energy range of 2000–2300 $cm^{-1}$, showed for all porosities the presence of relatively high intense peaks with some shifting, corresponding to Si-$H_x$ stretching band, characteristic of porous silicon, in good accord with the literature. In this range, the shift in the absorbance peak to higher wavenumbers, as the porosity increases, has been assigned to the different orientation of the pore shape created in the chosen supercell. In addition, the IR spectra obtained for different porosities show resemblance, on the one hand, between 15.62 and 40.62% porosities and, on the other hand, between 3.12 and 28.12% porosities with some shifting as reported.

Finally, the IR absorbance spectrum obtained for a porosity of 40.62% shows a good agreement with the experimental one.

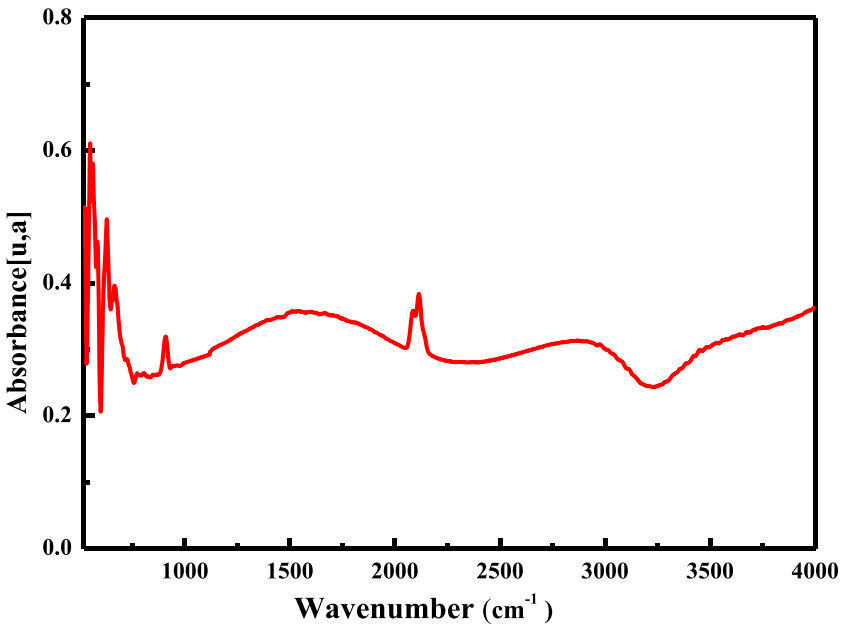


**Fig. 11** Experimental FTIR spectrum of porous silicon

**Acknowledgements** The authors are grateful to Mr. Mazari Redha from university of Medea for his helpful contribution in informatics assistance.

## References


1. Turner DS (1958) Electropolishing silicon in hydrofluoric acid solutions. J Electrochem Soc 105(1):402–408
2. Lowell S, Shields JE, Thomas MA, Thommes M (2004) Characterisation of porous solids and powders: surface area, porosity and density. Springer, Switzerland
3. Salonen J (2014) Drug delivery with porous silicon, Handbook of porous silicon, Leigh Canhan edit., Springer p.909
4. Belhousse S, Cheraga H, Gabouze N, Outemzabet R (2004) Fabrication and characterization of a new sensing device based on hydrocarbon groups (CHx) coated porous silicon. Sensors Actuators B 100:250–255
5. Canham LT (1990) Silicon quantum wire array fabrication by electrochemical and chemical dissolution of wafers. Appl Phys Lett 57: 1046
6. Klyshko A (2008) Mechanical strength of porous silicon and its possible applications. Superlattice Microst 44:374–377
7. Duttagupta SP, Chen XL, Jenekhe SA, Fauchetc PM (1997) Microhardness of porous silicon films and composites. Solid State Commun 101(1):33–37
8. Canham LT (2014) Mechanical properties of porous silicon. Handbook of porous silicon, pp 213–220
9. Berger MG, Frohnoff S, Theiss W, Rossow U, Munder H (1994) Porous silicon science and technology. Springer, Berlin, p 345
10. Chazalviel J-N, Etman M, Ozanam F (1991) A voltammetric study of the anodic dissolution of p-Si in fluoride electrolytes. J Electroanal Chem 297:533–540
11. Lehmann V (1993) The physics of macropore formation in low doped n-type silicon. J Electrochem Soc 140:2836
12. Slimani A, Iratni A, Chazalviel J-N, Gabouze N, Ozanam F (2009) Experimental study of macropore formation in p-type silicon in a fluoride solution and the transition between macropore formation and electropolishing. Electrochim Acta 54:3139–3144
13. Cheggou R, Kadoun A, Gabouze N, Ozanam F, Chazalviel J-N (2009) Theoretical modelling of the I–V characteristics of p-type silicon in fluoride electrolyte in the first electropolishing plateau. Electrochim Acta 54:3053–3058
14. Matthai CC, Gavartin JL, Cafolla AA (1995) Structural and elastic properties of porous silicon. Thin Solid Films 255(Issues 1–2):174–176
15. Romero C, Noyola JC, Santiago U, Valladares RM, Valladares A, Valladares AA (2010) A new approach to the computer modeling of amorphous nanoporous structures of semiconducting and metallic materials: a review. Materials 3:467–502
16. Clark SJ, Segall MD, Pickard CJ, Hasnip PJ, Probert MIJ, Refson K, Payne MC (2005) First principles methods using CASTEP. Z Kristallogr 220:567–570
17. Segall MD, Lindan PJD, Probert MJ, Pickard CJ, Hasnip PJ, Clark SJ, Payne MC (2002) First-principles simulation: ideas, illustrations and the CASTEP code. J Phys Condens Matter 14:2717
18. Calvino M, Trejo A, Iturrios MI, Crisóstomo MC, Carvajal E, Cruz-Irisson M (2014) DFT study of the electronic structure of cubic-SiC nanopores with a C-terminated surface. J Nanomater 2014
19. Trejo A, Calvino M, Ramos E, Cruz-Irisson M (2012) Computational simulation of the effects of oxygen on the electronic states of hydrogenated 3C-porous SiC. Nanoscale Res Lett 7:471
20. Trejo A, Calvino M, Cruz-Irisson M (2010) Chemical surface passivation of 3C-SiC nanocrystals: a first-principle study. Int J Quantum Chem 110:2455–2461
21. Monkhorst J, Pack JD (1976) Special points for Brillonin-zone integrations Hendrik. Phys Rev B 13(12)
22. Pfrommer BG, Côté M, Louie SG, Cohen ML (1997) Relaxation of crystals with the quasi-newton method. J Comput Phys 131:233–240
23. Fischer TH, Jan Almli W (1992) General methods for geometry and wave function optimization. J Phys Chem 96:9768–9774
24. Baroni S, de Gironcoli S, Dal Corso A, Giannozzi P (2001) Phonons and related crystal properties from density-functional perturbation theory. Rev Mod Phys 73
25. Selmane N, Cheknane A, Gabouze N, Maloufi N, Aillerie M (2017) Experimental study of optical and electrical properties of ZnO nano composites electrodeposited on n-porous silicon substrate for photovoltaic applications. E3S Web Conf 22:00155
26. Herino R, Bomchil G, Barla K, Bertrand C, Ginoux JL (1987) Porosity and pore size distributions of porous silicon layers. J Electrochem Soc 134(8):1994–2000
27. Lehman V (2002) Electrochemistry of silicon: instrumentation, science, materials and applications. Wiley-VCH, Weinheim. ISBN 3-527-29321-3
28. Sze SM (1969) The physics of semiconductor devices. Wiley, New York pp. 12-20
29. Cisneros R, Ramırez C, Wang C (2007) Ellipsometry and *ab initio* approaches to the refractive index of porous silicon. J Phys Condens Matter 19:395010
30. Lyer S, Xie Y-H (1993) Light emission from silicon. SCIENCE 260:40–46
31. Morán-López JL (1998) Current problems in condensed matter. Springer US
32. Cruz-Irissona M, Wang C (2009) Electronic and vibrational properties of porous silicon. J Nano R 5:153–160
33. Chuan FZ, Raphael T (1994) Porous silicon. World scientific
34. Alfaro P, Cisneros R, Bizarro M, Cruz-Irisson M, Wang C (2011) Raman scattering by confined optical phonons in Si and Ge nanostructures. Nanoscale 3:1246
35. Young TF, Chen CP, Liou JF, Chang TC (2000) Study on the vibrational state of the near surface region of porous silicon. J Porous Mat 7:339–343
36. Salcedo WJ, Fernandez FJR, Galeazzo E (1997) Structural characterization of photoluminescent porous silicon with FTIR spectroscopy. Braz. J Phys 27(4):158–161
37. Liua F-M, Rena B, Yana J-W, Mao B-W, Tian Z-Q (2002) Initial oxidation processes on hydrogenated silicon surfaces studied by in situ Raman spectroscopy. J Electrochem Soc 149(1):G95–G99
38. Palavicini A, Wang CM (2013) Infrared transmission in porous silicon multilayers. OPJ 3:20–25